Comments on Inorganic Chemistry
Publication details, including instructions for authors and subscription information:
http://www.informaworld.com/smpp/title~content=t713455155

Scanning Tunneling Microscopy of Molecular Adsorbates

HÉCtor D. Abruña[a]; Joachim Hossick Schott[b]; James E. Hudson[a]; Shelly R. Snyder[b]; Henry S. White[c]
[a] Department of Chemistry, Cornell University, Ithaca, New York [b] Department of Chemical Engineering and Materials Science, University of Minnesota, Minneapolis, Minnesota [c] Department of Chemistry, University of Utah, Salt Lake City, Utah

To cite this Article Abruña, HÉCtor D. , Schott, Joachim Hossick , Hudson, James E. , Snyder, Shelly R. and White, Henry S.(1994) 'Scanning Tunneling Microscopy of Molecular Adsorbates', Comments on Inorganic Chemistry, 15: 3, 171 — 196
To link to this Article: DOI: 10.1080/02603599408035842
URL: http://dx.doi.org/10.1080/02603599408035842

Scanning Tunneling Microscopy of Molecular Adsorbates

HÉCTOR D. ABRUÑA,* JOACHIM HOSSICK SCHOTT,†
JAMES E. HUDSON,* SHELLY R. SNYDER†
and HENRY S. WHITE**

* *Department of Chemistry,*
Cornell University,
Ithaca, New York 14853

†*Department of Chemical Engineering and Materials Science,*
University of Minnesota,
Minneapolis, Minnesota 55455

**Department of Chemistry,*
University of Utah,
Salt Lake City, Utah 84112

Received August 16, 1993

The recent development of scanning tunneling microscopy (STM) and tunneling spectroscopy (TS) has allowed the electronic and atomic structure of interfaces to be probed with unprecedented spatial resolution. Although both STM and TS are now commonly used in investigations of metal and semiconductor surfaces, these techniques can also be applied in chemical investigations of molecular species and molecular films, frequently providing details of their orientation, density, and electronic properties. In this review, the instrumentation and fundamental principles underlying STM and TS are presented and recent examples of STM/TS investigations of molecular interfaces are described. Emphasis is placed on investigations of molecularly thin films of electroactive transition metal complexes, e.g., [(Ru(terpyridine))$_2$(tetrapyridylpyrazine)]-(PF_6)$_4$ and protoporphyrin(IX)-Fe(III)Cl, deposited on metal and graphite electrodes. In addition, studies of quasi-crystalline molecular films, silver halide films, and surface defects are also presented to dem-

Comments Inorg. Chem.
1994, Vol. 15, Nos. 3 & 4, pp. 171–196
Reprints available directly from the publisher
Photocopying permitted by license only

onstrate the broad range of chemical systems that can be explored by these techniques.

Key Words: *scanning tunneling microscopy, tunneling spectroscopy, electrochemistry, molecular films, chemical dynamics*

INTRODUCTION

The control and understanding of interfacial reactivity at the atomic and molecular levels would profoundly affect many areas of scientific, technological and economic importance. Attainment of this goal is largely dependent on our ability to establish correlations between interfacial structure and reactivity.

The recent advent of Scanning Tunneling Microscopy (STM), Atomic Force Microscopy (AFM), and related scanned-probe techniques and the ability to visualize molecular structures with atomic resolution has captured the imagination of the scientific community and, at the same time, has revolutionized the field of surface science and provided an extraordinary new impetus to microscopy. Most STM work to date has been focused primarily on topographical studies of metal and semiconductor surfaces. Since the STM tip follows the contours of constant electron density at a particular energy (which is largely determined by the difference in Fermi energies between the tip and the substrate surface), variation of the bias voltage allows tunneling through different molecular energy states.

There are a number of areas in interfacial science that stand to benefit greatly from the application of STM and related techniques. Of these, electrochemistry appears to be uniquely positioned due to the fact that the electrode potential can be employed as a means to control and/or alter the distribution of charge of atomic or molecular species as well as to induce changes in the surface morphology of a material. In addition, it has been shown that the STM can operate in the presence of an electrolyte solution.[1] A number of in-situ and ex-situ STM studies of electrochemical systems have recently appeared. These include studies of electrode topography, oxide and metal film growth and the deposition of adatoms on single crystal surfaces.

In this brief account we will present a general overview of STM

and how it can be employed in the study of systems of interest to the inorganic chemistry community. A number of representative examples will be used to demonstrate the broad range of materials that can be characterized by this new technique.

SCANNING TUNNELING MICROSCOPY AND TUNNELING SPECTROSCOPY

The heart of the STM is the tip, a metal wire that ideally terminates in a single atom (Fig. 1). Using a sensitive stepping motor and piezoelectric transducers, the STM tip can be positioned within a nanometer of the sample surface. At this distance, the electron orbitals of the sample and tip overlap slightly and a tunneling current, of the order of nanoamperes (10^{-9} amp), flows when a small voltage bias is applied between the tip and the sample. The tunneling current has an approximately exponential dependence on the distance between the tip and the sample; variations of the tunneling gap by ~1 Å result in an order of magnitude change in the tunneling current. This sensitive dependence of the current on the tip-sample separation provides STM with its high resolving power; particularly in the direction normal to the surface.

To obtain an image of the sample, the tip is rastered across the

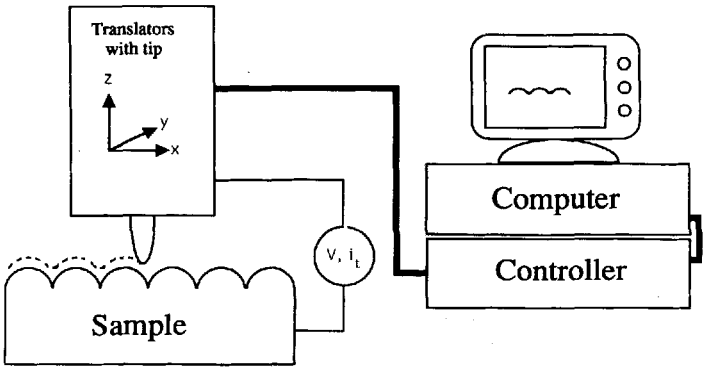

FIGURE 1 Schematic representation of the scanning tunneling microscope.

sample surface using a piezoelectric crystal, a material that expands with applied voltage. As the tip moves across the sample surface, topographical features on the surface cause fluctuations in the tunneling current. These fluctuations can be used to construct STM images in one of two ways. In the first mode, referred to as constant-height imaging, the STM tip is kept at a constant height above the sample and the tunneling current is plotted as a function of position. However, due to the fact that the tip–sample separation remains constant (once it is established at the beginning of a scan), this mode of operation is impractical for highly stepped surfaces, since it frequently results in the tip impacting the sample. In the second mode, referred to as constant-current imaging, the tunneling current is held constant as the tip is rastered across the surface. Thus, the tip follows contours of constant tunneling current. Constant-current imaging is accomplished through the use of an electronic feedback loop that senses changes in the tunneling current and moves the tip closer to or further away from the surface in order to maintain a constant tunneling current. An image can then be generated by plotting the tip deflection as a function of position.

Since STM is sensitive to the electron density contours of the surface, images are strongly dependent on the structural arrangement of atoms and molecules, as well as on several experimental parameters, e.g., voltage bias and tip–sample distance, that can be externally controlled. Unfortunately, theories describing their effects on experimental observation are still very rudimentary.[2] Because of similarities at the microscopic level, electron tunneling processes that occur during STM imaging of electroactive molecules have a *conceptually* similar basis as electron-transfer reactions that take place in conventional electrochemical reactions.[3,4] In the electrochemical experiment, electron-transfer occurs between an electrode surface and an electroactive molecule (within a layer of solvent molecules and ions which create the electrical double layer at the electrode–solution interface). In the STM experiment, electron-transfer takes place between a metal tip and the substrate coated with a molecular adsorbate. In either experiment, the tunneling current, I, can be expressed as:

$$I = \int_0^{eV} \rho_s(E)\rho_t(E, eV)T(E, eV)dE \qquad (1)$$

where $\rho_s(E)$ is the combined density of states of the substrate *plus* adsorbate, $\rho_t(E, \text{eV})$ is the density of states of the tip in the case of a vacuum junction or the solution density of molecular states next to the electrode in the case of an electrochemical interface, and $T(E, \text{eV})$ is the transmission probability for electrons crossing the tunneling barrier.[5] Equation (1) was applied as early as 1931 by Gurney[6] in establishing a quantum-mechanical basis for the observed non-linear electrochemical *I-V* characteristics. For the case of tunneling across a vacuum junction, the density of states of a metallic tip, $\rho_t(E, \text{eV})$, is usually taken to be nearly constant over the full range of bias voltages used.[7]

The combined density of electronic states, $\rho_s(E)$, associated with a molecular film *plus* substrate can be experimentally evaluated by measuring the dependence of the tunneling current I on the applied voltage, V, while the tip is stationary. Such an experiment is referred to as tunneling spectroscopy (TS). As shown by Feenstra and co-workers, $\rho_s(E)$ can be obtained by differentiation of Eq. (1) to yield

$$\rho_s(E) \sim (dI/dV)(I/V)^{-1} \tag{2}$$

where $(dI/dV)(I/V)^{-1}$ represents the differential conductance (dI/dV) of the tunnel junction normalized to the total or integral conductance (I/V). The right-hand side of Eq. (2) can be numerically evaluated from experimental *I-V* data to the yield the $\rho_s(E)$ associated with the adsorbate-covered substrate. This method of analyzing for $\rho_s(E)$ yields tunneling spectra (i.e., plots of $(dI/dV)(I/V)^{-1}$ vs. V) that are approximately independent of the tip-to-substrate separation.

ELECTROACTIVE MOLECULAR FILMS

The structure and properties of electroactive molecular films is often controlled by the chemical and physical properties of the metal on which the film is deposited. In addition, metal surfaces can be quite heterogeneous with features in the STM response that can easily, and incorrectly, be assigned to adsorbed molecules. Thus, interpretation of STM images of molecular adsorbates is

generally accompanied by detailed studies of the substrate prior to deposition of the molecule. The entire STM experiment usually involves three experimental stages: (i) STM characterization of the uncoated surface, prior to and after its immersion in the *pure* solvent to be used for adsorption of the molecular species; (ii) adsorption or electrodeposition of the molecular species; (iii) STM characterization of the adsorbed film, either dried (in air or vacuum) or *in-situ* (with the sample immersed in the solvent). The following example illustrates the importance of careful characterization of the uncoated substrate.

Substrate Induced Ordering of Molecular Adsorbates

A particularly interesting feature of the Au(111) surface is that it has two stable structures at room temperature. The first is the 1 $\times$ 1 unreconstructed Au(111) surface, representing an almost ideal termination of the bulk lattice. This surface is readily imaged by STM in air or vacuum. Images of such a surface display the characteristic hexagonal atomic arrangement (Au has an fcc structure) of Au atoms expected for an ideal (111) surface. The second structure is the so-called $\sqrt{3} \times 22$ reconstructed surface, which results from the rearrangement of the Au atoms in the topmost atomic layer. Generally, surface reconstructions occur to relieve stresses in the surface layer. For Au(111), the surface stress is partly alleviated by the insertion of one extra atom every 22 atoms in the $\langle 110 \rangle$ direction.[8] The increased atom density of the surface layer results in a slight "buckling" of the surface. Thus, STM images of the reconstructed Au surface exhibit parallel pairs of corrugation lines with a horizontal pair-to-pair separation of ~65 Å and a vertical corrugation amplitude of ~0.2 Å (Figs. 2a and 2b).

Topographical features, such as the parallel pairs of corrugation lines, are thought to be accompanied by changes in the surface electron density profile.[9] Therefore, molecular adsorbates may be expected to decorate the surface in a way which reflects these local variations in the surface electron density. This is indeed observed in the STM images shown in Figs. 2c and 2d. Upon exposure of a reconstructed ($\sqrt{3} \times 22$) Au(111) surface to a millimolar solution of $[(Ru(bpy)_2(bpy\text{-}(CH_2)_x\text{-}bpy)]^{2+}$ (x = 4,5) in dimethylformamide, the adsorbed molecules assemble on the surface with a long

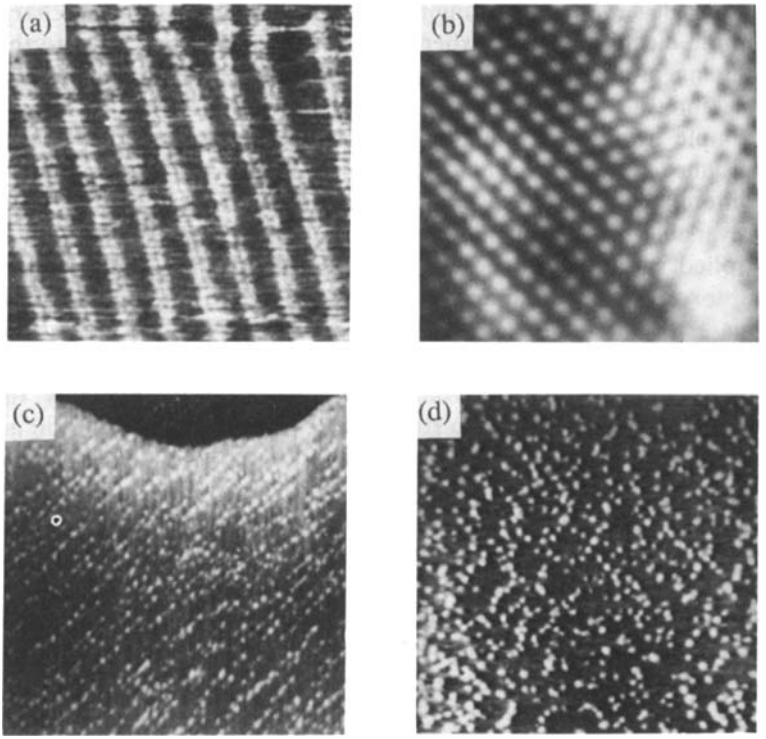

FIGURE 2 (a) STM image of an annealed Au(111) surface showing parallel line pairs of the $\sqrt{3} \times 22$ reconstruction. (b) STM image ($\sim 3 \times 3$ nm) showing the atomic arrangement within the reconstructed phase. STM images (150×150 nm) of adsorbed films of $[(Ru(bpy)_2(bpy\text{-}(CH_2)_x\text{-}bpy)]^{2+}$ on the (c) $\sqrt{3} \times 22$ reconstructed and (d) unreconstructed Au surfaces. The adsorbed films on the reconstructed surface display highly ordered patterns that are commensurate with the measured corrugation pattern of the substrate.

range order, reflecting the underlying reconstructed surface. Conversely, adsorption of $[(Ru(bpy)_2(bpy\text{-}(CH_2)_x\text{-}bpy)]^{2+}$ on the unreconstructed (1×1) surface results in a completely random adsorption pattern.[10]

Transitions between the unreconstructed and reconstructed surface phases can occur but require the input of an activation energy by thermal or electronic means. *Reversible* surface phase transitions between the reconstructed and the unreconstructed phases

can be observed upon changing the sign of the excess surface charge in the electrochemical experiment.[11] It is interesting to note that the magnitude of the electric field at a conventional electrochemical interface (10^6–10^7 V/cm) is similar to that between the tip and sample in an STM. In the latter experiment, the tip-to-sample distance is of the order of 5 Å and the tip-to-sample potential difference is 0.05 to 0.5 V. Consequently, it is possible to facilitate reversible phase transitions of the bare Au(111) surface by controlled variations of the tip–sample voltage bias. This is indeed observed in STM experiments.[12] Scanning with negative sample biases ($V_b < -0.5$ V) induces the $(1 \times 1) \rightarrow (\sqrt{3} \times 22)$ reconstruction, whereas the reverse transition $(\sqrt{3} \times 22) \rightarrow (1 \times 1)$ is observed at positive bias voltages ($V_b > +1$ V). Interestingly, this mechanism can be used to study order–disorder transitions in adsorbate layers of $[(Ru(bpy)_2(bpy\text{-}(CH_2)_x\text{-}bpy)]^{2+}$ on Au(111). Upon scanning at a sample bias of -1.5 V, the initially disordered adsorbate layer of $[(Ru(bpy)_2(bpy\text{-}(CH_2)_x\text{-}bpy)]^{2+}$ on the initially unreconstructed surface is transformed into the more ordered adsorbate layer. This result is easily understood. Scanning with a high negative sample bias reconstructs the initially unreconstructed substrate surface, which in turn forces the molecular adsorbate layer to reassemble in a long-range ordered pattern.

Polymerization Mechanisms

Electroreduction of $[Re(CO)_3$(4-vinyl,4′-methyl-2,2′-bipyridine)-Cl] (abbreviated hereinafter as $[Re(CO)_3(vbpy)Cl]$) at highly ordered pyrolytic graphite (HOPG) electrodes in acetonitrile yields a stable, electrochemically active polymer film that is capable of electrocatalytic and photoelectrocatalytic reduction of CO_2 to CO on metallic and semiconductor electrodes. The structure and chemical composition of thin films resulting from reductive polymerization of $[Re(CO)_3(vbpy)Cl]$ at metal electrodes depends on the experimental conditions at which reduction is performed. We have used STM to directly observe the polymer and potential-dependent variations in structure and morphology.[13]

Voltammetric studies indicate that the initial $1 - e^-$ reduction of $[Re(CO)_3(vbpy)Cl]$ at -1.45 V vs. SSCE (sodium saturated calomel reference electrode) yields the corresponding radical anion

(largely ligand localized) that polymerizes by chain propagation via linear vinyl–vinyl coupling of the vbpy ligand, i.e., $[Re(CO)_3(vbpy)Cl] + e^- \rightarrow [Re(CO)_3(vbpy)Cl]^-$. Repeated cycling of the electrode potential to -1.45 V results in deposition of an electroactive film. In addition to polymerization, slow loss of Cl^- from the electrogenerated radical anion accompanied by Re–Re bond formation has been demonstrated, i.e., $2\,[Re(CO)_3(vbpy)Cl]^- \rightarrow [(CO)_3(vbpy)Re-Re(CO)_3(vbpy)] + 2\,Cl^-$. It should also be mentioned that at potentials negative of -1.9 V the di-anion is generated. This species will rapidly lose chloride and dimerize. Depending on the potential range scanned and the scan rate employed in the electrodeposition, polymer films can be formed that are either predominantly polymerized monomer (bright yellow films) or mixtures of the monomer and dimer (greenish-yellow films).

Figure 3b shows an STM image of an HOPG electrode cycled between 0.05 V and -2.0 V in a solution containing $[Re(CO)_3(vbpy)Cl]$. The image exhibits molecules uniformly distributed over large regions of the surface. The discrete species were comprised of spheres ~16 Å in diameter; the predominant molecular form was a pair of spheres, separated by a distance of 6–7 Å, in a dumbbell shape. Based on geometric considerations, this entity was assigned as a tetrameric species, i.e., each lobe of the dumbbell was composed of two $Re(CO)_3(vbpy)$ units joined through a Re–Re metal bond and the two lobes were joined via vinyl–vinyl coupling.

Polymerization from vinyl–vinyl coupling of the radical anion results when the electrode potential is cycled between 0 and -1.45 V. Figure 3c shows spherical-shaped (200–300 Å diameter) polymeric deposits along several step sites on the surface. No deposits were observed on the substrate in regions removed from the steps, indicating that steps on the HOPG surface provide a significantly larger number of sites conducive to polymer nucleation. STM images of the spheres taken at higher magnification show they appear to be composed of fibrils ~8–10 Å in diameter.

Based on the above STM images and voltammetric results, a mechanism for polymerization vs. dimerization may be rationalized. Cycling the electrode potential between 0.0 and -1.45 V generates only the anion radical which will *slowly* lose chloride and dimerize. However, since the electron resides primarily in a

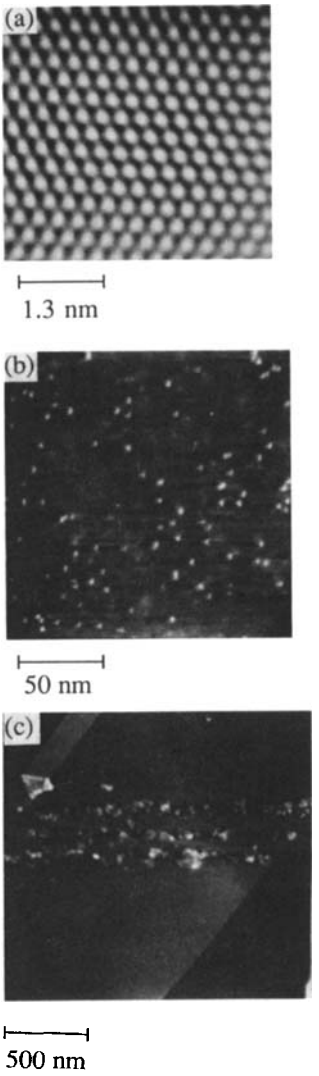

FIGURE 3 (a) STM image of a bare HOPG electrode. (b) STM image of a HOPG electrode after potential cycling between 0.0 and −2.0 V vs. SSCE in acetonitrile containing 2 m*M* [$Re(CO)_3(vbpy)Cl$] and 0.1 *M* TBAP. The 1900 × 1900 Å image shows uniform deposition of adsorbed molecules. (c) 17000 × 17000 Å STM image of polymer spheres nucleated along step sites on the HOPG surface.

ligand based orbital which is responsible for polymerization, and since chloride loss is slow, we are, in effect, favoring the rate of polymerization vs. that of dimerization. On the other hand, when the potential is scanned out to -2.0 V, the generated di-anion can *rapidly* lose chloride and dimerize. Such dimeric species, however, are expected to have more severe steric constraints for polymerization compared to the monomeric species. Thus, in this potential regime we, in effect, accelerate the dimerization pathway over polymer formation.

Adsorption of $[(Ru(terpy))_2(TPPZ)]^{+2}$

Because of its two terdentate binding sites, the ligand tetrapyridyl pyrazine (TPPZ) represents an excellent candidate for the preparation of homo and hetero multimetallic transition metal complexes with the potential for metal–metal interactions, and we have recently reported on the synthesis and characterization of a number of Ru and Os complexes of this ligand.[14] The large aromatic framework of TPPZ would be expected to enhance adsorption onto graphite as well as other surfaces, thus minimizing surface mobility. In addition, and as we have previously shown, complexes of TPPZ can undergo electroprecipitation as well as electropolymerization via the use of appropriately substituted ancillary ligands such as vinyl-terpyridine. In addition, the symmetry of the metal complexes could also favor dense packing, giving rise to ordered structures which provide for stability in STM imaging.

We have carried out a preliminary STM study of [(terpy)-Ru(TPPZ)Ru(terpy)]$(PF_6)_4$ (see Fig. 4 for structure) adsorbed onto HOPG. STM images of films of the complex in the sub-monolayer range show a high degree of organization (see Fig. 4). Molecular films are comprised of oblong-shaped structures whose dimensions were consistent with the anticipated geometric dimensions of the molecule (~26 Å × 13 Å). The molecules appear to be in a pseudo-rectangular packing arrangement with an inter-molecular spacing of 15 Å, consistent with the model of a closed-packed molecular film.

A more detailed investigation of these films, however, was hampered by degradation of the molecular packing order with scanning possibly due to the electric field surrounding the STM tip. Such

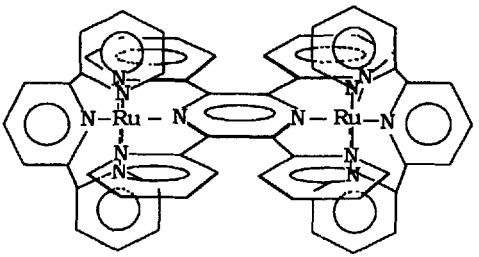

$[(Ru(terpy))_2TPPZ]^{+4}$

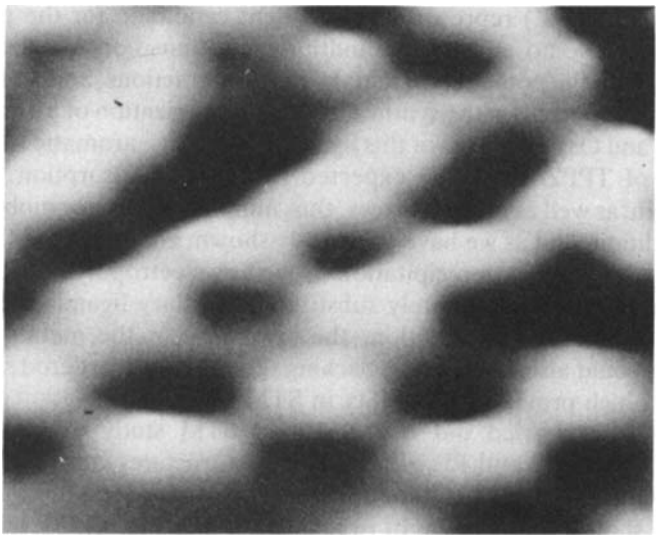

FIGURE 4 Top: Structure of $[(Ru(terpy)_2TPPZ)](PF_6)_4$. Bottom: STM image of the basal plane of a HOPG electrode after cycling the potential between 0.0 and −1.8 V vs. SCE in acetonitrile containing ~1 mM $[(Ru(terpy))_2(TPPZ)](PF_6)_4$ and 0.1 *M* TBAP. 70 × 70 Å image showing oblong-shaped molecules in a pseudo-rectangular packing arrangement.

degradation of structure with scanning is not unexpected since in this case the molecules are bound to the graphite surface only via van der Waals interactions. However, as mentioned above, we have also prepared the vinyl-terpyridine derivative which is electropolymerizable so that such degradation of structure with scanning could, in principle, be minimized or eliminated. We are currently characterizing these electropolymerized films by STM, AFM and TS.

Electrochemical Polymerization of $[Ru(bpy)_2(vpy)_2]^{+2}$

The complex $[Ru(bpy)_2(vpy)_2](PF_6)_2$, which contains two vpy (vinyl pyridine) ligands can be electropolymerized[15] to give both straight chain and branched polymers.[16] Figure 5 shows an STM image of the surface of an HOPG electrode after electropolymerization of $[Ru(bpy)_2(vpy)_2](PF_6)_2$ to a surface coverage of several equivalent monolayers. From the image, it can be seen that the electrode surface is covered with small spherical structures of the order of ~10 Å in diameter. Figure 5 also shows regions of the electrode surface where polymeric strands have deposited. The chain lengths vary from ~22 Å to ~55 Å. The dimensions of the strands suggest that they are a polymeric form of the complex, i.e., the polymer is one monomer unit in width and up to 5 monomer units in length. In addition to straight polymer chains, branching polymer chains are also evident. Analysis of the STM image shows that ~20% of the complexes imaged are in the polymerized form so that they appear as two or more spheres joined together. This small percentage of polymerized molecules may be due to the steric constraints imposed on the molecule by the presence of the two bipyridine ligands in addition to the two vinyl pyridine ligands.

As was the case for $[(Ru(terpy))_2TPPZ](PF_6)_4$, repeated STM imaging over regions where the complex had deposited resulted in their being swept to the sides (fringes) of the image. Even in the case where a polymer chain had deposited, it appears that the interaction of the chain with the basal plane of graphite is weak, giving rise to a high surface mobility. In addition, fields from the tip may also be responsible, at least in part, for the relatively high surface mobility of the polymer chain on the HOPG surface. The

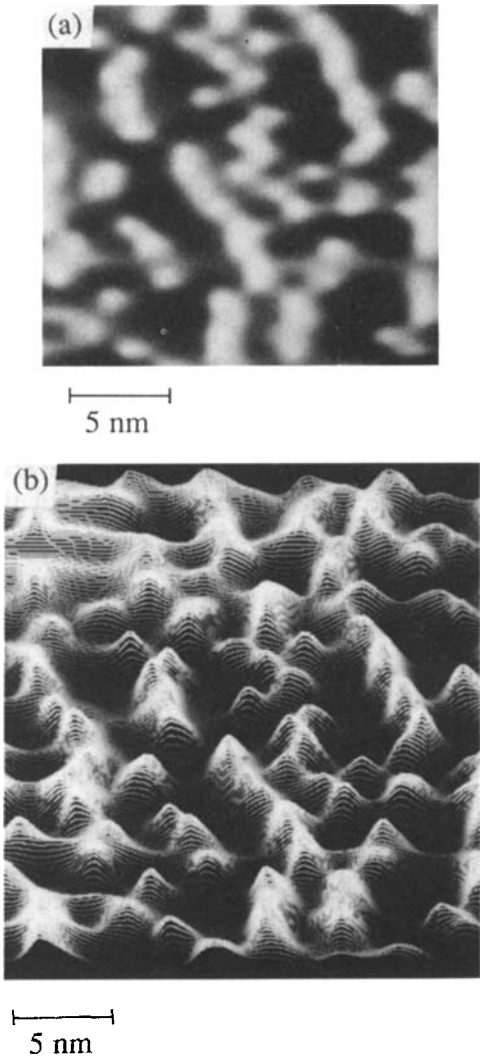

FIGURE 5 STM images of the basal plane of a HOPG electrode after cycling the potential between 0.0 and −1.75 V vs. SCE in acetonitrile containing ~1 mM $[Ru(bpy)_2(vpy)_2](PF_6)_2$ and 0.1 M TBAP. (a) 420 × 420 Å image showing the deposited complexes are composed of monomers and straight chain and branched chain polymers. (b) Tilted view showing the apparent film topography.

effects of forces between the tip and substrate are discussed in the final section of this article.

Electron-Transfer Studies of PP(IX)Fe(III)Cl Using STM

The adsorption and subsequent electrochemical behavior of PP(IX)-Fe(III)Cl on HOPG and glassy carbon electrodes has been investigated extensively. In aqueous solutions, PP(IX)Fe(III)Cl is known to form aggregates[17,18] as large as ~4,000,000 MW,[19] although typical values are in the range of ~30,000 MW.[20] The aggregates are thought to involve both μ-oxo bridged dimers[21] as well as larger oligomers where the complexes are associated through the vinyl groups,[22] and/or hydrogen bonded.[23]

The 0.25 μm^2 STM image in Fig. 6 shows an adsorbed PP(IX)Fe-(III)Cl film over large areas of the electrode surface. Two morphologically distinct regions of the film are apparent in Fig. 6. In the top half of the image, ~50 Å diameter, irregularly shaped aggregates of PP(IX)Fe(III)Cl are observed to be randomly distributed across the surface. In the lower half of the image, the film is comprised of molecular aggregates of similar size but which appear to be interconnected to form linear strands approximately

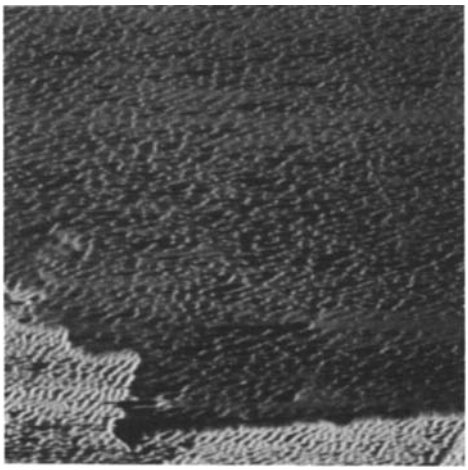

FIGURE 6 STM image (500 × 500 nm) of a PP(IX)Fe(III)Cl film on an HOPG electrode.

50 Å wide and of various lengths. In addition, the linear strands in the lower region are preferentially oriented (~45° with respect to the scan direction) suggesting either long range interaggregate ordering or a tip-induced ordering of aggregates. The lower region of the image is also displaced vertically by 20–30 Å relative to the upper region of the film, a finding that we attribute to the growth of a second layer of PP(IX)Fe(III)Cl aggregates over an underlying film or to an undetected crystallographic step on the underlying HOPG substrate.

Figure 7a shows a tunneling spectroscopy curve that was obtained on the adsorbed PP(IX)Fe(III)Cl film over the area where the smaller aggregates had deposited (top of Fig. 6). It is evident

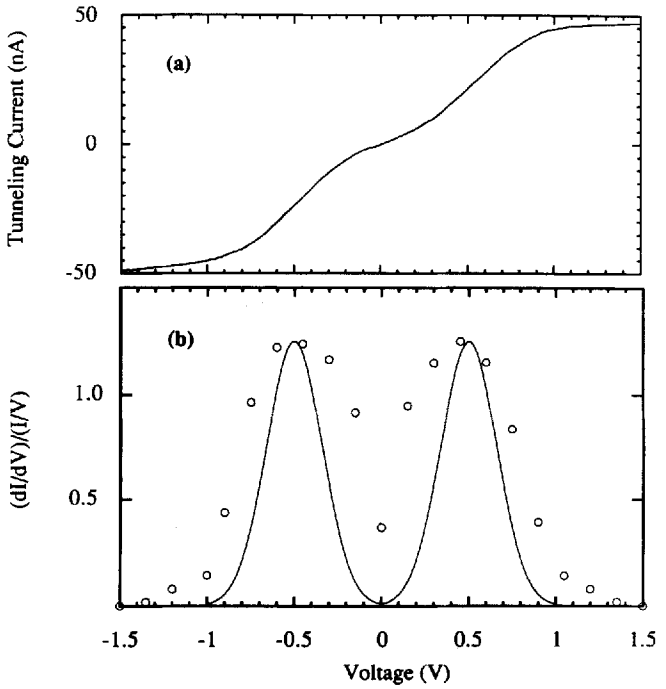

FIGURE 7 (a) *I-V* curve for a HOPG/PP(IX)Fe(III)Cl electrode. (b) $\rho_s(E)$ plot (dI/dV) vs. (V)) of the HOPG/PP(IX)Fe(III)Cl electrode from the data in (a) are shown as circles (○). The theoretical curve for $\rho_s(E)$ (solid line) is calculated from Eq. (5) in the text.

that the *I-V* curve is symmetric about 0.0 V. In addition, the tunneling current reaches a quasi-limiting value at biases larger than ± 1.0 V. The density of states, $\rho_s(E)$, calculated from these data are shown as open dots in Fig. 7b. Two quasi-bell-shaped peaks centered at ±0.5 eV are apparent in the TS data, representing the density of electronic states associated with electron tunneling processes of the HOPG/PP(IX)Fe(III)Cl structure at positive and negative biases. In contrast to the results obtained on the PP(IX)Fe(III)Cl film, $\rho_s(E)$ for the bare HOPG shows the density of states is described by an essentially broad continuum, in agreement with previous literature reports.

We propose that the general shape of the $\rho_s(E)$ plot measured for adsorbed PP(IX)Fe(III)Cl adsorbed on HOPG can be accounted for by assuming that the overall electron transfer mechanism between the STM tip and the underlying HOPG substrate occurs via a charge transfer mechanism mediated by adsorbed PP(IX)Fe(III)Cl. Our analysis explicitly assumes that redox reactions of the PP(IX)Fe(III)Cl film mediate the flux of electrons between the STM tip and substrate.

$$\text{PP(IX)Fe(III)Cl} + e^-_{\text{tip}} \rightleftharpoons \text{PP(IX)Fe(II)Cl} \qquad (3)$$

$$\text{PP(IX)Fe(II)Cl} \rightleftharpoons \text{PP(IX)Fe(III)Cl} + e^-_{\text{HOPG}} \qquad (4)$$

The subscripts "tip" and "HOPG" indicate the location of the transferring electron. Equations 3 and 4 are assumed to be reversible, allowing tunneling currents of equal magnitude to be observed at both positive and negative biases as is experimentally observed. The underlying assumption in proposing a redox mechanism (Eqs. (3) and (4)) is that the adsorbed PP(IX)Fe(III)Cl introduces a localized electronic state that is weakly coupled to the substrate and tip.

Assuming that electron-tunneling in the STM experiment occurs as a result of the two tunneling processes indicated in Eqs. (3) and (4), the experimentally obtained surface density of states, $\rho_s(eV)$ (see Eqs. (1) and (2)) can be compared with theoretical predictions of the classical Marcus model which describes the polarization-dependent density of states associated with a redox couple in terms

of the reorganizational energy, λ, and the standard potential of the redox couple, V^o. In the simplest form of this theory, the density of states is given by

$$\rho_s(E) = \Theta \exp[-(\lambda \pm e(V - V^o))^2/(\lambda 4kT)] \quad (5)$$

where Θ is a constant proportional to the number of electroactive species within electron-transfer distance of the electrode. The distribution function given by Eq. (5) predicts that the densities of electronic states associated with the reduced and oxidized halves of an electrochemically active molecule are described by symmetric gaussians displaced from V^o by $\pm\lambda/e$. The magnitude of λ reflects the energy associated with reorganization of the solvent upon change of the oxidation state of the molecule and with molecular structural changes accompanying electron transfer, and has been the focus of numerous recent studies concerned with the dynamics of homogeneous and heterogeneous electron-transfer reactions. Morisaki and co-workers have directly evaluated ρ_s(eV) for several inorganic and organic molecules through tunneling spectroscopic measurements using macroscopic electrodes and have found their results to be in good agreement with Eq. (5).[24]

Theoretical values of $\rho_s(E)$ calculated from Eq. (5) using λ = 0.5 eV and V^o = 0.0 eV are shown as the solid line in Fig. 7b. Comparison of the experimental and theoretical values shows that the data are in reasonable agreement with theory although a true gaussian distribution is not observed. The widths of the ρ_s(eV) curves are $\sim 2\lambda$ in agreement with theoretical expectations.

The shape of the SDOS plots suggests that the PP(IX)Fe(III)Cl molecules that comprise the electroactive film are solvated to the extent that the molecules can be reduced or oxidized. The absence of a bulk solvent in the experiment, however, prevents any further analysis of the significance of λ. The value of $\lambda = \pm 0.5$ eV, which fits the experimental data in Fig. 7b, is well within the range of values (0.3 to 1.5 eV) measured for both inorganic and organic redox systems. Although it is unlikely that a continuous film of H_2O is present on the surface after air-drying the electrodes, we speculate that the individual molecules and residual electrolyte ions (Na^+ and $B_4O_7^{2-}$) that comprise the film may retain their solvation shells in the absence of rigorous drying.

It is possible to convert the tunneling current measured in the STM or TS experiments to an absolute electron-transfer rate constant, assuming that the dimensions and shape of the tunnel junction are known. Calculated values of k_{et} (10^9–5×10^{10} s^{-1}) obtained in the tunneling measurements for PP(IX)Fe(III)Cl films are of the same order of magnitude as recently reported values of the first-order rate constants for exothermic electron-transfer reactions between dissimilar electroactive molecules separated by a saturated hydrocarbon spacer.[25,26] Although obvious physical and chemical differences exist between the mechanisms of electron transfer involved in the STM experiment and in the purely chemical systems, the conceptual similarity between these reactions and the order-of-magnitude agreement in the observed rates suggests that STM can be employed to investigate the dynamics of extremely fast electron transfer reactions.

CRYSTALLINE FILMS

Halogen Adlayer Structure on Ag Surfaces

The structure of halogen adlayers on Ag surfaces is of fundamental interest in electrochemistry and photography. We have recently developed a method of preparing atomically smooth adlayers of F, Cl, Br, and I (and mixtures of different halogen atoms) on Ag(111) surfaces, allowing real-space atomically resolved structures of these adsorbed layers to be obtained using STM.[27] The structures we have obtained are consistent with previous LEED and SEXAFS data; however, new atomic level features in the adlayer structure are readily discernible in the real-space STM images.

STM images of the halogen-coated Ag surfaces show atomically flat terraces of widths up to 100 mm and separated from neighboring terraces by monoatomic steps of 3.0 Å average height. Figure 8 shows high-resolution STM images of all of the halogen adlayers. In each case, the coverage of halogen atoms corresponded to ~1 monolayer, as determined by Auger spectroscopy.

An interesting and systematic progression is observed in the

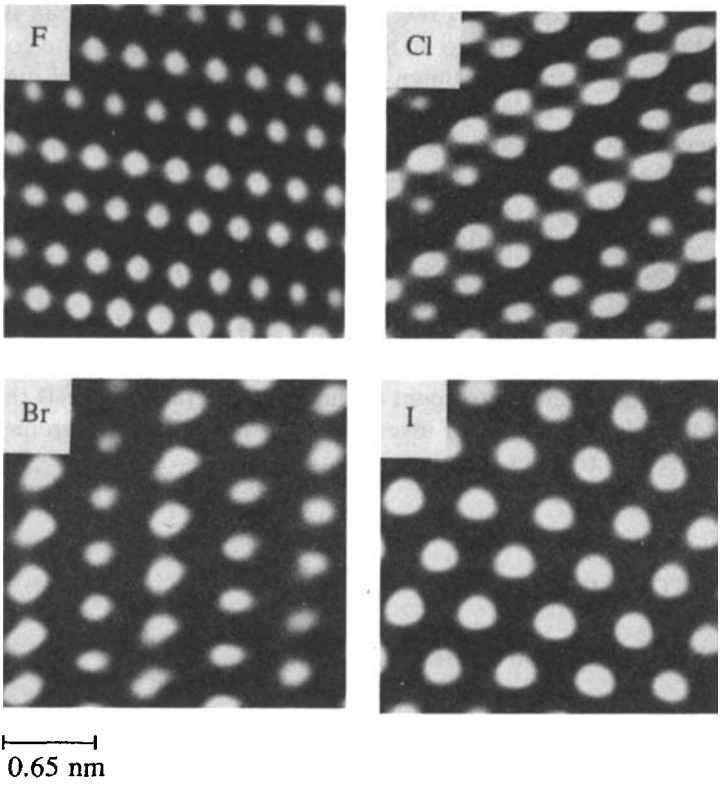

FIGURE 8 Atomically resolved images of halogen adlayers on Ag(111).

adlayer structure of the halogen adlayers (Fig. 8). The F adlayer is characterized by a complex double-row structure, which is readily apparent in the STM image. The interatomic dimensions are 2.8, 3.0, and 4.2 ± 0.2 Å. The Cl adlayer is qualitatively similar to F, with interatomic dimensions of 4.1, 3.3, and 3.8 ± 0.2 Å. For Br adlayers, the double row structure is noticeably less pronounced (interatomic spacings of 5.3, 5.1, and 4.4 ± 0.2 Å). For I, the double row structure is entirely absent, and the monolayer closely resembles the well-known $\sqrt{3} \times \sqrt{3}$/R30 adlayer structure (interatomic spacings of 4.9 and 4.6 ± 0.2 Å).

The above images suggest that the relative degree of symmetry

within the halogen adlayer increases with decreasing adatom electronegativity and increasing atom size. The atomic row arrangements of the F and Cl atoms likely reflect asymmetric lateral coulombic forces between localized charges. For I, the relative degree of charge delocalization is lower, and, hence, the degree of polarization is lower.

Because of the coupling between topographical and electronic effects, it is often difficult to correlate the grey-scale contrast observed in STM images with the absolute size of molecules and atoms. However, the STM images of the series of halogen atoms show that the trend in atomic dimensions is consistent with that expected based on tabulated crystallographic data for alkali halides, i.e., the apparent size of I adatoms is roughly twice that of F adatoms, with Cl and Br having intermediate values. The apparent sizes of the adatoms vary significantly from experiment to experiment, most likely due to differences in the shape of the STM tip. Nonetheless, the trend is encouraging and suggests that quantitative analyses of molecular structures are possible by STM. A detailed study of the interatomic distances, measured by STM, demonstrates that the halogen adatoms are ionic.[28]

It is also possible to image adlayers comprised of mixtures of two different types of halogen atoms.[28] For instance, Fig. 9 shows a mixed layer of I and F atoms on the Ag(111) surface. The structure of the mixed layer is significantly different from that of films comprised of only F or I. In addition to the normal periodicity at the atomic level, the mixed layers show a longer range periodicity. Figure 9a shows a quasi-hexagonal long range order in the F/I atom layer that we have interpreted to arise from a lattice mismatch between the Ag and halogen layer. It is interesting to note that the mixed layers also display a larger number of point defects (Fig. 9b) that represent missing atoms in the film. We speculate that this defect results from stresses in the film that occur either as the result of the lattice mismatch or from coulombic forces between ionic adatoms.

Results from tunneling spectroscopic experiments of the halogen-coated Ag surfaces are also particularly interesting.[29] Sharp maxima are observed in the *I-V* spectra that have been assigned

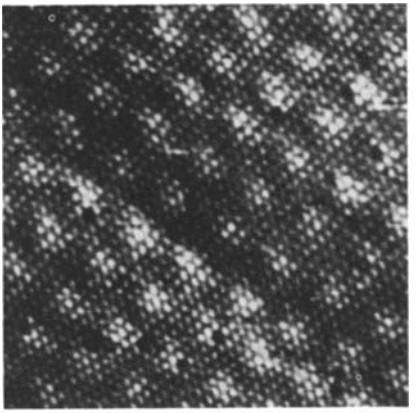

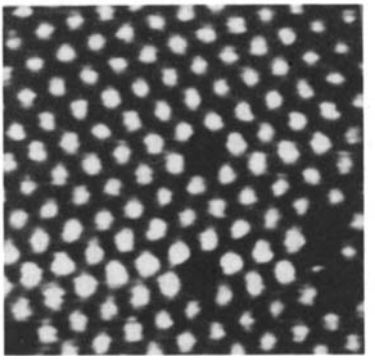

FIGURE 9 (*Top*) Images of mixed monolayer of I and F on Ag(111); (*bottom*) atomic vacancies in the mixed monolayer.

to resonance tunneling through the occupied p- and virtual bound states of individual halogen atoms. Diode-like electrical behavior is observed for these single atom tunnel junctions, illustrating the use of STM to study the electrical properties of interfaces at the atomic level.

INTERACTIONS OF THE STM TIP WITH THE SAMPLE

In STM experiments, the tip must interact with the sample in order to generate an image. If the interaction is large, it is possible that the sample surface will be altered. As noted in some of the previous examples, we frequently observe in studies of molecular films that the STM tip will sweep molecules out of the region being investigated. The final example, although not concerned with molecular films, is included to illustrate tip–sample interactions.

Highly oriented pyrolytic graphite (HOPG) has been used extensively as a substrate in STM investigations because it is readily cleaved to yield atomically flat stable surfaces. HOPG samples are comprised mainly of sheets of hexagonal graphite. However, based on transmission electron microscopy, Lipson and Stokes[30] reported in 1942 that natural graphite samples are comprised of 5–15% rhombohedral graphite, intermixed with the more abundant hexagonal graphite. The percentage of rhombohedral graphite in synthetic HOPG, commonly used in STM studies, depends on the annealing and quenching procedures used in the specimen preparation, and is typically of the order of a few percent.[31,32] Rhombohedral graphite differs from hexagonal graphite in the stacking of atomic planes parallel to the *c*-axis. Rhombohedral graphite has an *abcabc* stacking sequence while hexagonal graphite has an *abab* stacking sequence. The rhombohedral phase is contained within stacking faults in pyrolytic graphite. The stacking faults are generally observed in TEM as networks of *partial dislocations* that separate regions of faulted (rhombohedral) and unfaulted (hexagonal) graphite. By displacement of one or more atomic plane(s) normal to the *c*-axis, the transition between the rhombohedral and hexagonal phases within the network may be represented as *ababa* $\rightleftarrows$ *abcabc*. An in-plane transition between the two phases requires distortion of the atomic arrangement rather than actual bond breakage.

Figure 10a shows an STM image of a triangular-shaped network of partial dislocations on an HOPG surface.[33] Based on the structural assignments from previous TEM and electron diffraction analyses,[34,35] and the geometrical similarity of the network array in both STM and TEM images, the lighter triangles in the STM images are assigned the rhombohedral crystal structure and the

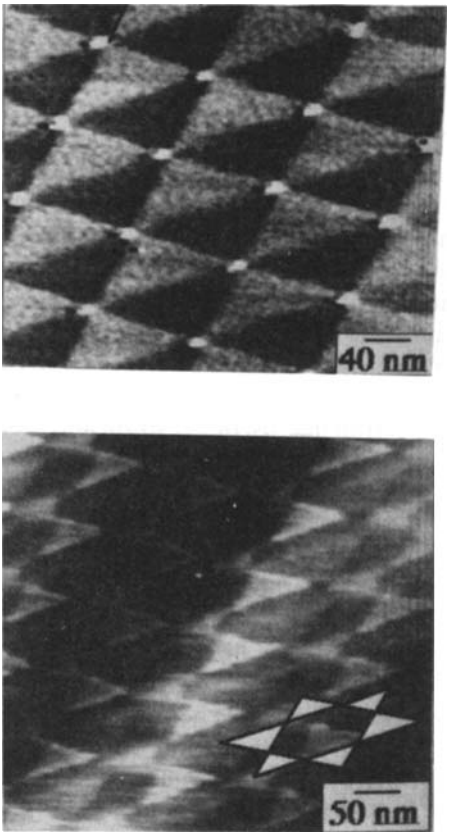

FIGURE 10 STM image of a 400 nm × 400 nm area of (*top*) triangular and (*bottom*) star-shaped arrays on the (0001) plane of HOPG. The array consists of alternating faulted (rhombohedral graphite, light triangular regions), and unfaulted (hexagonal, dark triangles).

darker triangles the hexagonal crystal structure. On average, the bases and heights of the triangles were 75 and 110 nm, respectively. The triangular network for this HOPG sample encompassed a total area estimated to be in excess of 4 μm^2.

A *reversible* transformation of the triangular-shaped network to a star-shaped network was observed while varying the STM bias voltage between 0.24 and 0.1 V, with the tunneling current maintained at 2.4 nA. Figure 10b shows a 500 mm × 500 nm stable

image of the dislocation network several minutes after the bias had been decreased from 0.24 V to 0.1 V. The network now appears to consist of alternating small and large triangles oriented at 180° from one another in the form of a distorted star. The sum of the lengths of the bases of small and large triangles (31 and 45 nm, respectively) is equivalent to the length of the base of an individual triangle (75 nm) in the network in Fig. 10a. A similar equivalence exists between the heights of the triangles.

The mechanism for the transition between network geometries undoubtedly involves the movement of dislocations within the network. The transition can be viewed as resulting from the concerted motion of parallel dislocations along one of the three equivalent ⟨10$\bar{1}$0⟩ directions. Indeed, STM images verified that motion of only one set of parallel partial dislocations occurred during the transition.[33] Not coincidentally, motion occurred only for dislocations, oriented nearly at right angles to the direction in which the tip was scanning (consistent with the notion that motion results from tip-induced shear stress). The reversibility of the transition also suggests that one of the two metastable states (triangles vs. stars) results from a cancellation of shear forces and restoring forces that result from a local distortion of the network.

The shear force necessary to induce the reversible transition between the star and triangular-shaped dislocation arrays results from the STM tip scanning over the HOPG surface. The magnitude of this force can be determined from a detailed analysis of the relative energies of the dislocation arrays and is estimated to be 5 MPa.[33] Forces of this magnitude are expected to easily disrupt the structure of molecular films, and therefore must be considered in the analysis of STM images.

Acknowledgments

The authors are grateful to the Office of Naval Research, the National Science Foundation and the Materials Science Center at Cornell University.

References

1. T. Hachiya and K. Itaya, Ultramicroscopy, **42–44**, 445 (1992), and references therein.

2. Lang, N. D. Phys. Rev. B **37**, 10395 (1988).
3. J. K. Sass and J. K. Gimzewski, J. Electroanal. Chem. **251**, 241 (1988).
4. G. Travaglini, M. Amrein, B. Michel and H. Gross, in *Scanning Tunneling Microscopy and Related Methods*, eds. R. J. Behm *et al.* (Kluwer Academic Publishers, Netherlands, 1990), p. 335.
5. I. Giaever, Phys. Rev. Lett. **5**, 464 (1960).
6. R. W. Gurney, Proc. Royal Soc. (London) **134A**, 137 (1932).
7. S. Park, J. Nogami, H. A. Mizes and C. F. Quate, Phys. Rev. B **38**, 4269 (1988).
8. J. V. Barth, H. Brune, G. Ertl and R. J. Behm, Phys. Rev. B **42**, 9307 (1990).
9. R. Smoluchowski, Phys. Rev. **60**, 661 (1941).
10. J. Hossick Schott, C. R. Arana, H. D. Abruña, H. H. Petach, C. M. Elliot and H. S. White, J. Phys. Chem. **96**, 5222 (1992).
11. X. Gao, A. Hamelin and M. J. Weaver, J. Chem. Phys. **95**, 6993 (1991).
12. J. Hossick Schott and H. S. White, Langmuir **8**, 1955 (1992).
13. S. R. Snyder, H. S. White, S. Lopez and H. D. Abruña, J. Am. Chem. Soc. **112**, 1333 (1990).
14. C. R. Arana and H. D. Abruña, Inorg. Chem. **32**, 194 (1993).
15. H. D. Abruña, P. Denisevich, M. Umaña, T. J. Meyer and R. W. Murray, J. Am. Chem. Soc. **103**, 1 (1981); P. Denisevich, H. D. Abruña, C. R. Leidner, T. J. Meyer and R. W. Murray, Inorg. Chem. **21**, 2153 (1982); H. Abruña, Coordination Chemistry Reviews **86**, 135 (1988).
16. C. M. Elliott, C. J. Baldy, L. M. Nuwaysir and C. L. Wilkins, Inorg. Chem. **29**, 389 (1990).
17. O. K. Medhi and J. Silver, Inorganica Chimica Acta **153**, 133 (1988).
18. W. I. White, *The Porphyrins*, ed. D. Dolphin (Academic Press, New York, 1978), Vol. V, Ch. 7.
19. F. Haurowitz, Hoppe-Seyler's Z. Physiol. Chem. **254**, 266 (1938).
20. G. Blauer and B. Zvilichovsky, Arch. Biochem. Biophys. **127**, 749 (1968).
21. J. Shack and W. M. Clark, J. Biol. Chem. **171**, 143 (1947).
22. (a) W. A. Gallagher and W. B. Elliot, Ann. N. Y. Acad. Sci. **206**, 463 (1973); (b) P. Jones, K. Prudhoe and S. B. Brown, J. Chem. Soc. Dalton Trans. 911 (1974); (c) M. W. Makinen and W. A. Eaton, Ann. N.Y. Acad. Sci. **206**, 210 (1973).
23. R. Lemberg and J. W. Legge, *Hematin Compounds and Bile Pigments* (Wiley (Interscience), New York, 1979).
24. H. Morisaki, H. Ono and K. Yazawa, J. Electrochem. Soc. **137**, 2759 (1990).
25. A. D. Joran, B. A. Leland, P. M. Felker, A. H. Zewail, J. J. Hopfield and P. B. Dervan, Nature **327**, 508 (1987).
26. G. L. Closs and J. R. Miller, J. Am. Chem. Soc. **106**, 3047 (1984).
27. J. Hossick Schott and H. S. White, J. Phys. Chem., in press.
28. J. Hossick Schott and H. S. White, Langmuir, submitted.
29. J. Hossick Schott and H. S. White, J. Phys. Chem., submitted.
30. H. Lipson and A. R. Stokes, Proc. Roy. Soc. A **181**, 101 (1942).
31. G. Bacon, Acta Cryst. **3**, 320 (1958).
32. H. Jagodzinski, Acta Cryst. **2**, 298 (1949).
33. S. R. Snyder, W. W. Gerberich and H. S. White, Phys. Rev. B **47**, 10, 823 (1993).
34. P. Delavignette and S. J. Amelinckx, Nucl. Mater. **5**, 17 (1962).
35. G. K. Williamson, Proc. Roy. Soc. A **257**, 457 (1960).